A Section 508–conformant HTML version of this article is available at https://doi.org/10.1289/EHP9406.

Satellite-Based Long-Term Spatiotemporal Patterns of Surface Ozone Concentrations in China: 2005–2019

Qingyang Zhu,[1] Jianzhao Bi,[2] Xiong Liu,[3] Shenshen Li,[4] Wenhao Wang,[1] Yu Zhao,[5] and Yang Liu[1]

[1]Gangarosa Department of Environmental Health, Rollins School of Public Health, Emory University, Atlanta, Georgia, USA
[2]Department of Environmental & Occupational Health Sciences, School of Public Health, University of Washington, Seattle, Washington, USA
[3]Harvard–Smithsonian Center for Astrophysics, Cambridge, Massachusetts, USA
[4]State Key Laboratory of Remote Sensing Science, Institute of Remote Sensing and Digital Earth, Chinese Academy of Sciences, Beijing, China
[5]State Key Laboratory of Pollution Control and Resource Reuse and School of the Environment, Nanjing University, Nanjing, Jiangsu Province, China

Background: Although short-term ozone (O_3) exposure has been associated with a series of adverse health outcomes, research on the health effects of chronic O_3 exposure is still limited, especially in developing countries because of the lack of long-term exposure estimates.

Objectives: The present study aimed to estimate the spatiotemporal distribution of monthly mean daily maximum 8-h average O_3 concentrations in China from 2005 to 2019 at a 0.05° spatial resolution.

Methods: We developed a machine learning model with a satellite-derived boundary-layer O_3 column, O_3 precursors, meteorological conditions, land-use information, and proxies of anthropogenic emissions as predictors.

Results: The random, spatial, and temporal cross-validation R^2 of our model were 0.87, 0.86, and 0.76, respectively. Model-predicted spatial distribution of ground-level O_3 concentrations showed significant differences across seasons. The highest summer peak of O_3 occurred in the North China Plain, whereas southern regions were the most polluted in winter. Most large urban centers showed elevated O_3 levels, but their surrounding suburban areas may have even higher O_3 concentrations owing to nitrogen oxides titration. The annual trend of O_3 concentrations fluctuated over 2005–2013, but a significant nationwide increase was observed afterward.

Discussion: The present model had enhanced performance in predicting ground-level O_3 concentrations in China. This national data set of O_3 concentrations would facilitate epidemiological studies to investigate the long-term health effect of O_3 in China. Our results also highlight the importance of controlling O_3 in China's next round of the Air Pollution Prevention and Control Action Plan. https://doi.org/10.1289/EHP9406

Introduction

Numerous epidemiological studies have shown that short-term ozone (O_3) exposure is associated with a series of adverse health outcomes, including all-cause nonaccidental mortality (Yin et al. 2017) and respiratory morbidity (Barry et al. 2019). In 2015, O_3 pollution contributed to an estimated 9–23 million asthma emergency department visits globally (Anenberg et al. 2018). A handful of studies have also investigated the chronic health effects of O_3, but their conclusions differed, as reviewed by Nuvolone et al. (2018). For example, Turner et al. (2016) reported a positive association between long-term O_3 exposure and all-cause mortality in a large prospective study in the United States. However, a meta-analysis reported that this association existed only in the warm season rather than the whole year (Atkinson et al. 2016). One potential reason for this inconsistency was the bias in the exposure matrices, especially in large long-term studies. Seltzer et al. (2018) highlighted the value of a dense monitoring network in measuring long-term O_3 exposure, but such a network is unavailable in most developing countries. As the world's most populous nation, China began to establish its national air quality monitoring network in 2013. To date, this network covers most Chinese cities, but the rural and suburban areas remain largely unmonitored (Xiao et al. 2020). The insufficient spatiotemporal coverage of O_3 measurements presents a major hurdle to retrospective epidemiological studies in China, especially those established before the 2010s (Wang et al. 2017).

Satellite remote sensing has become a promising tool to extend the records of O_3 measurements in space and time. For example, the Ozone Monitoring Instrument (OMI) is a nadir-viewing ultraviolet (UV)-visible (270–550 nm) solar backscatter spectrometer aboard the National Aeronautics and Space Administration (NASA) Aura satellite designed to measure the total O_3 column and other trace gases (Levelt et al. 2006). Since its launch in July 2004, researchers have been exploring ways to estimate boundary-layer O_3 levels using the OMI and other satellite data. Based on the OMI's measurements, Liu et al. (2010a) developed an optimal estimation technique to retrieve the O_3 profile from the surface to ~60 km to produce the Smithsonian Astrophysical Observatory (SAO) OMI Ozone Profile (OMPROFOZ) product. The OMPROFOZ product has been shown to capture enhancements of lower tropospheric O_3 over China (Shen et al. 2019) and East Asia (Hayashida et al. 2015), but its performance varies in space and by season owing to various factors affecting the horizontal and vertical distribution of tropospheric O_3 (Huang et al. 2017). In China, the daily correlation between the OMPROFOZ tropospheric column and ground-level O_3 measurements varies from <0.1 in high-latitude regions to >0.6 in low-latitude regions (Shen et al. 2019).

Surface-level O_3 is formed by complex photochemical reactions between volatile organic compounds (VOCs) and nitrogen oxides (NO_x) in the presence of heat and solar radiation (Li et al. 2020; Pu et al. 2017). In addition to the abundance of precursors, the production of surface O_3 can be strongly influenced by meteorology. For example, high temperature boosts O_3 chemistry by increasing the decomposition rate of peroxyacytyl nitrate (PAN), thus preventing the sinkage of NO_x and peroxyl radicals (Fischer et al. 2014; Lu et al. 2019a). Water vapor may affect surface O_3 production by modulating the hydrogen oxide (HO_x) radicals essential to O_3 production from oxygen (Lu et al. 2016). Besides these persistent effects, lightning would result in a surge in NO_x emission, significantly elevating short-term ground-level O_3 concentrations (DeCaria et al. 2005; Kang et al. 2020).

Address correspondence to Yang Liu, Gangarosa Department of Environmental Health, Rollins School of Public Health, Emory University, 1518 Clifton Rd., Atlanta, GA 30322 USA. Email: yang.liu@emory.edu

Supplemental Material is available online (https://doi.org/10.1289/EHP9406).

All authors declare they have no actual or potential competing financial interests.

Received 29 March 2021; Revised 9 January 2022; Accepted 12 January 2022; Published 9 February 2022.

Although photochemical reactions predominantly determine tropospheric O_3 concentrations (Lelieveld and Dentener 2000; Monks 2005), in some circumstances the stratospheric O_3-rich air may penetrate rapidly into the lower troposphere and cause a sharp increase in ground-level O_3 pollution (Knowland et al. 2017). The peak of this cross-tropopause mass transport, known as a stratospheric intrusion (SI), in the northern hemisphere usually occurs in springtime, especially in high-altitude regions, such as the Qinghai-Tibet plateau (Appenzeller et al. 1996; Itahashi et al. 2020; Lin et al. 2012; Lu et al. 2019b; Wang et al. 2020b). Changes in large-scale climate patterns, such as El Niño, are associated with increased SIs and surface O_3 concentrations (Shen and Mickley 2017; Xie et al. 2014). In addition, vegetation has complicated effects on surface O_3. On one hand, plants can remove surface O_3 through dry deposition (Clifton et al. 2020); however, on the other hand, plants may emit VOCs to the atmosphere and affect O_3 pollution (Kigathi et al. 2019). Therefore, land cover types are also important in determining ambient O_3 concentrations.

In this study, we developed a national-scale machine learning model to estimate historical ambient ground-level O_3 concentrations in China at a monthly level from 2005 to 2019 at a 0.05° spatial resolution. In addition to the OMPROFOZ O_3 profile, we included meteorological factors, land-use information, O_3 precursors, and indicators of anthropogenic emissions to account for the complicated formation and removal processes of surface O_3. We first present our model development strategy, then evaluate model performance using statistical techniques, as well as ground measurements not included in model training. Finally, we investigate the spatiotemporal trend of O_3 and discuss the drivers of these patterns.

Data and Methods

Model Development

We used a random forest framework to estimate monthly mean daily maximum 8-h average (MDA8) O_3 concentrations in China from 2005 to 2019. The overall study workflow is illustrated in Figure S1. Briefly, we first extracted the fraction of the boundary-layer O_3 column from the OMPROFOZ O_3 profile. The depth of this layer for each grid cell was determined dynamically by the tropopause pressure (Liu et al. 2010a). Missing fraction values were imputed with daily random forest models incorporating the Modern-Era Retrospective Analysis for Research and Applications (MERRA-2) meteorological fields and surface flux. The gap-filled boundary-layer O_3 fractions were then used to calculate the full-coverage boundary-layer O_3 column (in Dobson units). The surface-level monthly average MDA8 O_3 concentration was generated by a separate random forest model trained with the gap-filled boundary-layer O_3 column, meteorological fields, land-use terms, elevation, and population density. The details of these predictors are described below.

Ground O_3 Measurements

Ground-level monitoring data from 2013 to 2019 were obtained from the China National Environmental Monitoring Center (CNEMC; http://www.cnemc.cn/). China's national air quality monitoring network measures hourly O_3 concentrations with either UV absorption (for point analyzers) or differential optical absorption spectroscopy (for open-path analyzers). MDA8 O_3 concentration was defined as the maximum 8-h moving average O_3 concentration (containing at least six valid hourly values) within a calendar day. We chose to use MDA8 rather than MDA1 or 24-h average because MDA8 has been widely used in O_3 health effects research (Lu et al. 2020; Lyu et al. 2019).

The quality assurance of the CNEMC data was conducted primarily based on its official standard (CNEMC 2012). Briefly, a valid 8-h moving average O_3 concentration must contain at least six hourly measurements. No regulatory standard has yet been set up for MDA8 O_3, but 20 hourly measurements were generally required for daily air pollutant concentrations. Therefore, we also removed all the observations during a given day from the stations with <15 hourly measurements to balance data abundance and data quality. A total of 2,443 (3%) monthly MDA8 O_3 concentrations were removed from the data set.

We further separated rural stations from urban stations to test our model performance in different settings. In compliance with China's official regulations (NBS 2008), we defined areas with a population density of $<1{,}500/\text{km}^2$ ($\sim$37,500 per grid cell) as rural. Consequently, 406 monitoring stations of 1,532 (27%) were identified as rural stations, contributing to a total of 24,405 (31%) data points. Note that population density is not the only determinant of rural/urban status listed in China's official standards. We used population to identify rural/urban stations primarily because other economic and political determinants were less quantifiable in this modeling study.

O_3 monitoring data from before 2014 was obtained from the Tropospheric Ozone Assessment Report (TOAR) (Xu et al. 2020). This data set contains MDA8 O_3 concentrations from eight different stations, including Mt. Waliguan (WLG, located at 36.30°N, 100.9°E), Shangdianzi (SDZ, at 40.39°N, 117.00°E), Lin'an (LAN, at 30.30°N, 119.73°E), Longfengshan (LFS, at 44.73°N, 127.60°E), Xianggelila (XGLL, at 28.01°N, 99.68°E), Akedala (AKDL, at 47.10°N, 87.93°E), Gucheng (GCH, at 39.13°N, 115.67°E), and China Meteorological Administration (CMA, at 39.95°N, 116.32°E). The locations of the TOAR sites can be found in Figure S2. The TOAR historical monitoring data was not used to train the final model but, rather, served as an independent external validation data set.

Satellite Remote Sensing Data

In this study, we used the OMI OMPROFOZ product developed at the Harvard SAO, publicly available at the NASA Aura Validation Data Center (AVDC). The O_3 profile is retrieved at 24 layers ($\sim$2.5 km per layer) from the surface to $\sim$65 km from the spectral range 270–330 nm, using the optimal estimation approach. It is based on the initial retrieval algorithm of Liu et al. (2010a) with modifications described by Kim et al. (2013). The layers between the surface and the tropopause were defined on a daily basis. That is to say, the layers' pressure boundaries were initially set at $P_i = 2^{-i/2}$ atm for $i = 0$–23, and $P_{24} = 0$. For each individual day, the National Centers for Environmental Prediction (NCEP) tropopause pressure were used to replace the pressure level closest to it. The layers between the surface and the tropopause were then reassigned based on equal logarithmic pressure intervals (Liu et al. 2010a). OMPROFOZ's retrieval errors due to precision (instrument random noise) and smoothing errors (insufficient vertical resolution) ranged from 1–6% in the stratosphere to 6–35% in the troposphere. The retrieval was performed at a spatial resolution of $52 \times 48\ \text{km}^2$ at nadir and gridded to a 0.5° resolution for ease of use.

For more intuitive interpretations, we defined OMPROFOZ's boundary layer (from surface pressure to $\sim$700 hPa) as Layer 24 (L24). Correspondingly, L23–L1 represents the second-lowest layer to the top layer. Our model initially used the boundary-layer (L24) partial column O_3 from the OMPROFOZ O_3 profile. To better understand OMPROFOZ's role in modeling long-term O_3 pollution, we also tested whether using additional tropospheric

columns (i.e., the summation of L22–L24) or replacing the retrievals with an *a priori* O_3 profile (both L24 and the summation of L22–L24) would influence the model performance.

Tropospheric column nitrogen dioxide (NO_2) concentration from 2005 to 2019 was extracted from the OMI global NO_2 product named OMNO2d (Krotkov et al. 2017). It provides global daily tropospheric column NO_2 concentration at a 0.25° resolution. We extracted the tropospheric column NO_2 concentration with cloud screening (i.e., pixels with a cloud fraction >30% were removed for quality assurance) as a measurement of O_3 precursor in the present study.

MERRA-2 Assimilated Data

We used the MERRA-2 meteorological data in the present study. The MERRA-2 provides the latest NASA atmospheric reanalysis data starting from 1980. It has a native resolution of $0.5° \times 0.625°$ and 72 vertical layers (Gelaro et al. 2017). We extracted surface-level meteorological fields, as well as those between surface and 150 hPa, to account for the effects of stratospheric intrusion (Knowland et al. 2017). The detailed list of MERRA-2 meteorological and chemistry fields we used is provided in Table S1.

Lightning Flash Density

Previous studies have shown that lightning flash is an important enhancer of tropospheric O_3 because of its considerable contribution to NO_x (DeCaria et al. 2005; Finney et al. 2016), especially in springtime (Lu et al. 2019b). We obtained global monthly lightning flash density data from the Harvard-NASA Emissions Component at a $0.5° \times 0.625°$ resolution, adopting an optimal regional scaling algorithm to reduce the bias of satellite-driven tropical lightning data (Murray et al. 2012).

South and Southeast Asia Wildfire

The massive human-initiated biomass burning in South and Southeast Asia greatly enhances springtime O_3 pollution over China, especially in the southwest (Ni et al. 2018; Wang et al. 2011). To test whether incorporating foreign wildfire data would increase model performance, we obtained the Moderate Resolution Imaging Spectrometer (MODIS) daily active fire data from 2005 to 2019 via the Fire Information for Resource Management System (FIRMS) data achieve (NASA Earthdata 2019). Fire points from 10 South and Southeast Asian countries—namely, Bangladesh, Bhutan, Cambodia, India, Laos, Myanmar, Nepal, Pakistan, Thailand, and Vietnam—were selected to capture most fire points in China's southern neighbors. Fire radiative power (FRP) was used as a quantitative proxy of fire-related emissions (Li et al. 2019a; Wooster et al. 2003).

Land Use, Population, Road Length, and Digital Elevation

Annual land cover maps were obtained from the European Space Agency (ESA) Climate Change Initiative (CCI) (ESA 2017) for 2005–2015 and the Copernicus Climate Change Service (C3S) Climate Data Store (CDS) for 2016–2019 (CDS 2021). The C3S land-use product used the same methodology as the ESA CCI land cover maps to guarantee long-term continuity, according to the product manual (C3S 2021). Both products provide 23 types of land cover at a spatial resolution of 300 m.

LandScan global population data were obtained from the Oak Ridge National Laboratory (https://landscan.ornl.gov/). This data set provides annual population density from 2005 to 2019 at a 1-km resolution. Road networks were obtained from the Global Roads Open Access Data Set (CIESIN and ITOS 2013). This data set was compiled from sources before 2010 (specific date unavailable). Total road length was included in our model as a proxy of traffic emissions. We also used 30-m elevation data from the Advanced Spaceborne Thermal Emission and Reflection Radiometer (ASTER) Global Digital Elevation Model (GDEM), version 3 (NASA and METI 2019). This latest version of ASTER GDEM has increased accuracy compared with previous versions.

Missing Value Imputation

Equation 1 Illustrates the relationship between the total column O_3 and the boundary-layer (L24) column O_3.

$$C_{PBL} = f_{PBL} \times C_{total}, \quad (1)$$

where C_{PBL} denotes the boundary-layer column O_3 (in Dobson units); f_{PBL} is the boundary-layer fraction of total column O_3; and C_{total} is the total column O_3. The OMPROFOZ product has a nonnegligible portion of missing values that will reduce the spatial coverage of f_{PBL} and affect predicted ground-level O_3 concentrations. We first filled the data gap of OMI f_{PBL}, then multiplied it with MERRA-2 C_{total} to get the final C_{PBL}. We chose this approach over directly imputing the OMPROFOZ product because OMI total O_3 column and Microwave Limb Sounder (MLS) stratospheric O_3 profiles have been assimilated into the MERRA-2 data after 2004 (Wargan et al. 2017). The correlation coefficient between MERRA-2 column O_3 and OMI column O_3 concentration was 0.97 in the present study. The missing values of OMI f_{PBL} were imputed with random forest models that incorporated MERRA-2 meteorological fields and surface flux measurements. These models were trained on a daily basis at the native resolution of the OMPROFOZ product.

Other OMI-derived partial column O_3 concentrations were processed similarly. To specify, missing values in other retrieved partial column O_3 concentrations were imputed independently with the same process to the boundary layer but with different meteorological fields corresponding to their pressure levels (i.e., 500–700 hPa for L23, 350–500 hPa for L22). The *a priori* O_3 profile (L22, L23, and L24) was processed independently but with the same methodology as the retrieved O_3 profile.

Data Integration

We created a 0.05° resolution modeling grid across China for data integration and model construction (Figure 1). A 50-km buffer region was added to China's national boundaries to ensure data sensitivity at the border area. The total number of grid cells was 399,513. Three megacity clusters were selected to study the regional patterns of O_3 pollution—namely, the North China Plain (NCP), the Yangtze River Delta (YRD), and the Pearl River Delta (PRD). We used an inverse distance weighting method to resample data at a spatial resolution coarser than 0.05°, including all OMI-derived column O_3 concentrations, tropospheric column NO_2 concentrations, MERRA-2 meteorological fields, and lightning flash density. In addition, we calculated the percentage coverage of different land-use categories, average elevation, total road length, and total population for each pixel. Daily data were then aggregated to the monthly level. Population and land use were processed at the annual level, whereas elevation and road length were fixed during the entire study period. After data integration, we selected grid cells that contained air quality monitoring stations to generate the training data set. All valid ground-level MDA8 O_3 observations within each grid cell were averaged on a monthly basis to match other model parameters.

The foreign wildfire data was processed in a different way because our study domain did not extend to China's neighboring countries other than the buffer area. We assumed that the foreign fire points have an additive and distance-dependent influence on China's O_3 concentrations. Therefore, the contributions of the

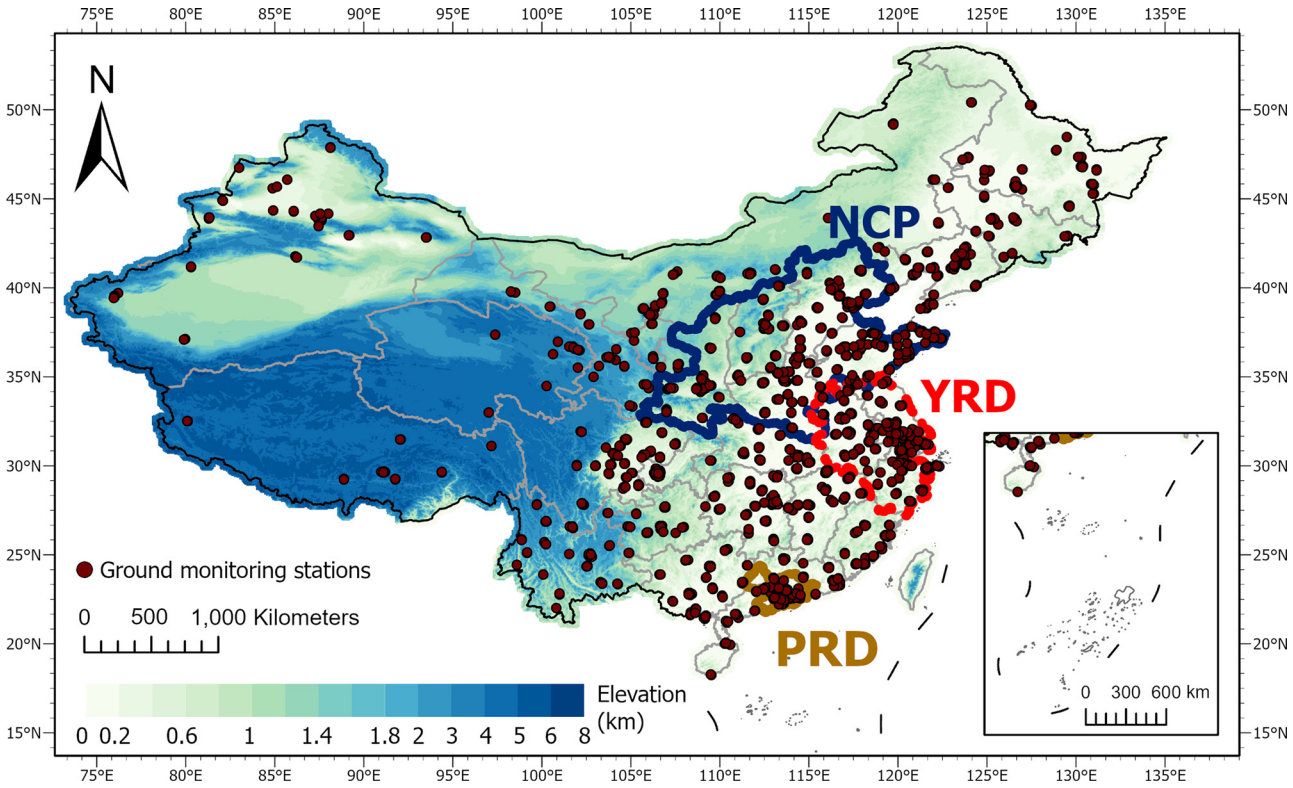

Figure 1. The study domain and three major city clusters. The study domain covered China plus a 50-km buffer region that extends outside the national boundary. The points are the location of the China National Environmental Monitoring Center monitoring sites. The color scale represents elevation (km). Note: NCP, North China Plain; PRD, Pearl River Delta region; YRD, Yangtze River Delta region.

South and Southeast Asian countries were quantified with the equation below (Equation 2).

$$FFE_{it} = \sum FRP_{jt} \times (dist_{ij})^{-2}, \quad (2)$$

where FFE_{it} denotes the influence of foreign fire emissions on grid cell i at day t; FRP_{jt} represents the FRP for fire point j at day t; and $dist_{ij}$ is the distance between fire point j and grid cell i.

Model Training, Validation, and Parameter Comparison

We divided the study period into the training period (2014–2019) and the hindcast period (2005–2013). The year 2013 was excluded from model training owing to fewer numbers of O_3 monitors and unstable data quality at the onset of the Chinese national monitoring network. We trained two separate random forest models with the same set of predictors for springtime (March–April–May) and the rest of the year because of the significantly different pattern of springtime O_3 in the northern hemisphere (Lin et al. 2012; Ni et al. 2018). To specify, the aforementioned rest of the year includes summer (June–July–August), fall (September–October–November), and winter (December–January–February). The detailed list of predictors included in our random forest models can be found in Table S1.

Note that some parameters were not included in the initial model. To specify, our original model was established with the boundary-layer (L24) column O_3 concentrations from the OMPROFOZ retrieved O_3 profile. The OMI L22–L24 retrieval and the *a priori* partial columns were used separately to compare model performance with different OMI-derived O_3 fields. In addition, the MODIS FRP was not initially used because it was generated completely outside of the study domain. Therefore, the original model hereafter represents the model with the retrieved O_3 profile L24 and without foreign fire emissions.

All models were validated with 10-fold random cross-validation (CV), that is, we randomly divided the original data set into 10 equal-sized subsets, used 9 of them to train a model, and made predictions on the left-out subset. This process was repeated 10 times so that each monthly mean MDA8 measurement would have a corresponding predicted value. Model performance metrics including R^2 and root-mean-square error (RMSE) were calculated using the measurement–prediction pairs. Similarly, we conducted a 10-fold spatial CV to test whether our model could make reliable predictions at locations without ground monitors. In the spatial CV, the original data set was randomly divided on the basis of each data point's location. Model predictions at a given location were generated by a model trained with data elsewhere. Finally, a temporal CV was conducted in which models trained for a given year would be validated with data from other years in the training period to test the reliability of model predictions in the hindcast period.

Given that each variable provides a different contribution to the overall model performance, the predictors' importance was evaluated with a permutation method (Altmann et al. 2010). Briefly, a variable's importance represents the percentage increase in the model's total mean squared error if this variable is replaced by its random permutation.

We used R (version 3.6.3; R Development Core Team) to process data and perform statistical analyses. Package *ranger* was used for training the random forest models.

Coupled Trend Evaluation between O_3 and fine particulate matter

To reduce severe air pollution, the State Council of China enacted the Air Pollution Prevention and Control Action Plan (APPCAP) in 2013. This policy has resulted in a substantial reduction in ambient fine particulate matter [PM $\leq$2.5 μm in aerodynamic

diameter ($PM_{2.5}$)], but the contemporary O_3 concentrations increased unexpectedly (Huang et al. 2018; Wang et al. 2020a). We obtained model-estimated nationwide $PM_{2.5}$ concentrations at a 1-km resolution (Liang et al. 2020; Xiao et al. 2021) to evaluate the nationwide long-term coupled change between O_3 and $PM_{2.5}$ under the APPCAP. The correlation between O_3 and $PM_{2.5}$ was examined with a partial correlation analysis, controlling for temperature, relative humidity, and total precipitation from MERRA-2.

Results

Model Performance and Parameter Comparison

The performance of the original model is illustrated in Figure 2. The predicted monthly average MDA8 O_3 concentrations from the combined springtime and non-spring model were in good agreement with the ground-based observations, with a random CV R^2 of 0.87 and an RMSE of 13.03 $\mu g/m^3$ (Figure 2A). The spatial CV had an almost identical performance with the random CV $R^2 = 0.86$, RMSE = 13.56 $\mu g/m^3$ (Figure 2B). The temporal CV had a slightly lower R^2 of 0.76 and a higher RMSE of 17.71 $\mu g/m^3$ (Figure 2C). The regression lines between the predicted and observed O_3 concentrations were close to the 1:1 line for all three types of CV.

As shown in Figure S3, replacing OMI L24 retrieval with the summation of L22–L24 retrievals would not substantially impact the model performance. The R^2 and RMSE were almost identical with the original model for all three CV types. Similarly, using the *a priori* O_3 profile (L24 or L22–L24) also had a minimum influence on the overall performance. Although using *a priori* L22–L24 would increase the temporal CV R^2 by 0.6%, such an attempt also had a negative impact on the predicted spatial distribution of O_3. Figure S4A shows an example of the spatial artifact (horizontal gap in the predicted O_3 concentrations) from the model with *a priori* O_3 profile L22–L24. This kind of artifact was not seen in the original model (Figure S4B). Given that using the alternative partial column O_3 amount would not improve the model performance, all results presented hereafter used the model with OMI L24 retrieval unless otherwise specified.

The season-specific model performance showed that our model had a lower performance in spring than in other seasons (Figure S5). To specify, the springtime R^2 were 0.72, 0.71, and 0.53 for random, spatial, and temporal CV, respectively. In addition, the RMSE for all types of CV in spring was around 3 $\mu g/m^3$ higher than in fall, but the overall O_3 concentrations were comparable in these two seasons.

In addition, our model performed better in urban regions than in rural regions (Figure S6). The random, spatial, and temporal CV R^2 were 0.88, 0.87, 0.76 in urban regions and 0.83, 0.81, 0.72 in rural regions. The prediction errors (i.e., RMSE) were also higher in rural regions than urban areas (1–2 $\mu g/m^3$ for all CV types).

Our predicted MDA8 O_3 concentrations also agreed well with the TOAR historical data monitoring data before 2014 (overall $R^2 = 0.73$, RMSE = 20.68 $\mu g/m^3$), except for the XGLL station. Site-specific time-series comparison (Figure S7) showed that the predicted O_3 trends were mostly identical with the observations at stations CMA, GCH, and LFS. Although our model may have underestimated O_3 concentrations at the LAN, SDZ, and WLG stations, especially in springtime, it still captured most of the O_3's temporal variation over these locations. The worst agreement was observed at the XGLL station, where our model had almost no sensitivity to the springtime peak O_3 concentrations. The monitoring data was mostly incomplete at the AKDL station, but it may also indicate some springtime underestimations in that region. Incorporating the MODIS FRP data would neither significantly improve the springtime nor the overall agreement with the TOAR historical data (Figure S8). Therefore, we excluded MODIS FRP from the model given that introducing data fields external to the study domain may incur unexpected uncertainty.

Although the OMI L24 retrieval had a low raw correlation with the CNEMC data ($R^2 = 0.34$, as presented in Figure S9), removing this parameter would result in a slight decrease in the model performance compared with the original model ($\sim 1\%$ decrease in R^2 for all three types of CV, as shown in Figure 2; Figure S10). Besides, the agreement between model predictions and the TOAR historical O_3 monitoring data would also be worse if OMI L24 retrieval is removed from the model (overall R^2 dropped from 0.73 to 0.70, RMSE increased from 20.68 to 22.38 $\mu g/m^3$) although the predicted temporal trends were generally similar (Figures S7 and S11).

Predictor Importance Ranking

Most of the top predictors in both the spring and non-spring models were meteorological factors, but their relative orders differed (Figure S12). Non-meteorological variables were more important in the non-spring model. For example, the five most important non-meteorological variables in the spring-excluded model were

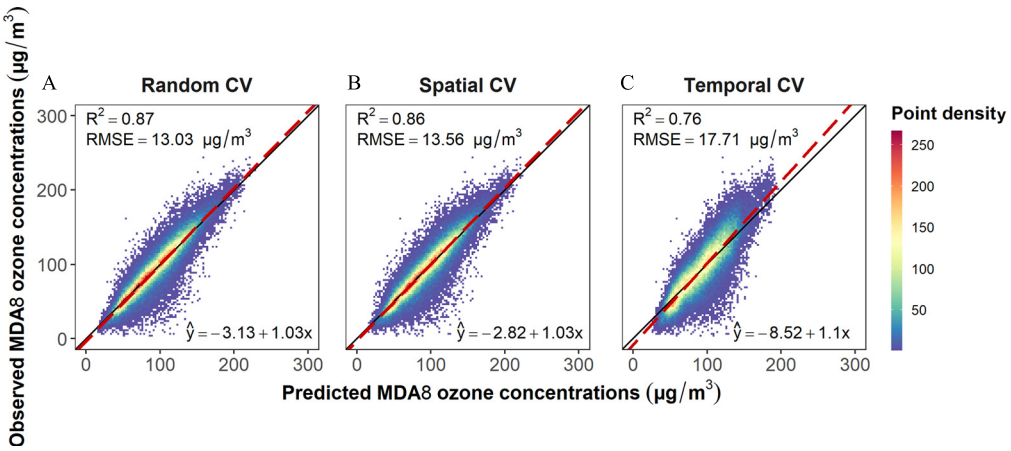

Figure 2. The integrated model performance of the original model with OMI L24 retrieval. (A) Random CV; (B) spatial CV; and (C) temporal CV. The functions on the bottom-right corners are the regression functions between the predicted and observed monthly mean MDA8 ozone concentrations. Red dashed lines represent the regression line between the predictions and observations; black solid lines represent the $x = y$ line. The color scale represents the density of the points. Note: CV, cross-validation; L24, boundary layer; MDA8, daily maximum 8-h average; OMI, Ozone Monitoring Instrument.

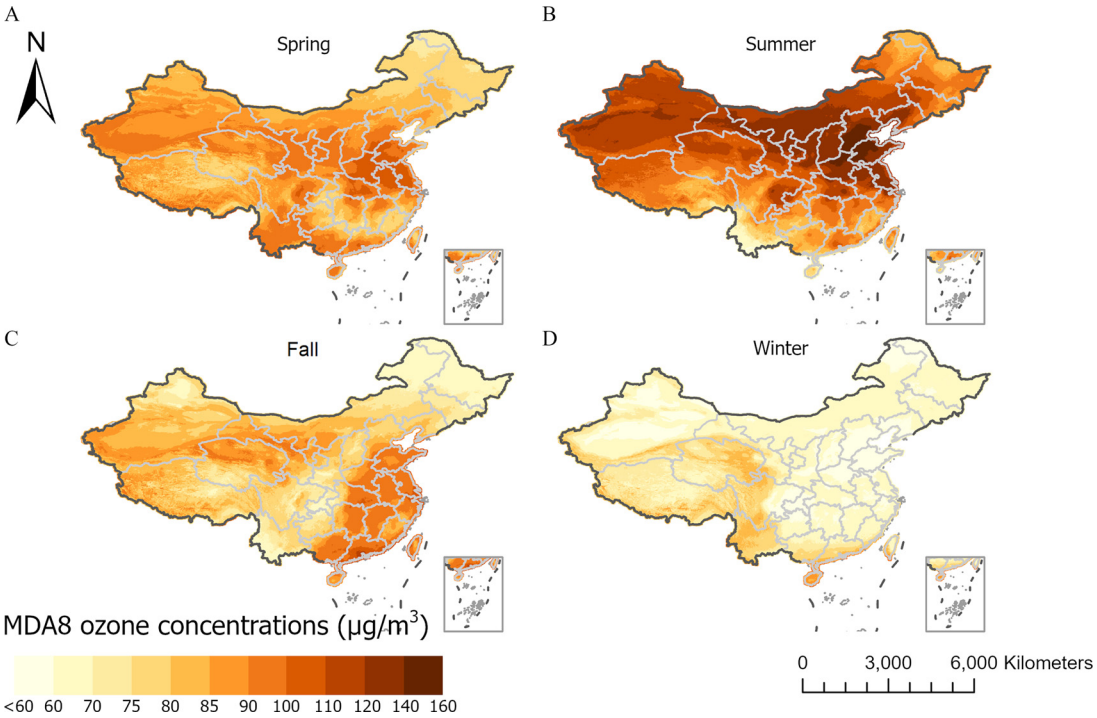

Figure 3. Spatial distribution of seasonal average MDA8 O_3 concentrations during 2005–2019. The O_3 concentrations were predicted by the original model with OMI L24 retrieval and averaged seasonally over 2005–2019. (A) Spring: March–April–May; (B) summer: June–July–August; (C) fall: September–October–November; and (D) winter: December–January–February. Note: MDA8, daily maximum 8-h average; O_3, ozone; OMI, Ozone Monitoring Instrument.

OMI NO_2, population, the proportion of rainfed cropland, irrigated or post-flooding cropland, and elevation. However, their importance ranking all dropped in the spring model. The gap-filled OMI boundary-layer O_3 was one of the most important variables in the spring model, and those that gained the most importance were associated with stratospheric intrusion (e.g., tropopause pressure and vertical wind columns) and lightning flash activity.

Seasonality and Spatial Heterogeneity of O_3 Levels in China

As shown in Figure 3, the spatial distribution and severity of surface O_3 pollution in China varied by season. The mean springtime MDA8 O_3 concentrations over 2005–2019 were mostly $\sim$80–90 $\mu g/m^3$. Moderate O_3 pollution ($\sim$100 $\mu g/m^3$) was observed in Central-East China, especially around the boundary region between the NCP and the YRD. Southwest China, including the Sichuan Basin and Yunnan Province, was also moderately polluted in this season (Figure 3A). In summer, heavy O_3 pollution was widespread in China, except for the southwest. The NCP had the worst O_3 pollution, with the highest 15-y mean MDA8 O_3 concentrations around Beijing approaching the national level-2 air quality standard (160 $\mu g/m^3$) (Figure 3B). In fall, the PRD region became the most polluted area after a sharp decrease in O_3 concentrations in North China (Figure 3C). Winter has the lowest O_3 levels, especially around the NCP region, and only the low-latitude regions may have an O_3 concentration approaching 100 $\mu g/m^3$ (Figure 3D).

Different regions appeared to have different seasonal patterns (Figure 4D). For example, O_3 concentrations in the NCP (Figure 4B) and nearby northern regions started to rise in spring and peaked in summer. After a sharp decrease in fall, these regions would have the lowest O_3 levels in the winter. In contrast, high O_3 concentrations could persist from spring to fall in southern China, without a clear peak in summer. Sporadic O_3 hot spots may even be found in winter (Figure 3D). The O_3 concentration in the YRD (Figure 4C) was a mixture of the two patterns above, that is, it had a flatter summer high and a winter low, but high O_3 concentrations also persisted in spring and fall. Most regions in China followed the aforementioned patterns, with a few exceptions. For example, Yunnan province saw O_3 levels peak in spring and then drop substantially in summer. O_3 concentrations on the Qinghai-Tibet plateau were relatively stable throughout the year, with only a mild peak occurring in summer.

O_3's spatial heterogeneity was observed not only nationwide but also at the city level. Figure 5A shows the model-estimated O_3 concentrations in the YRD region in August 2019, whereas Figure 5B shows population densities. Some population centers, such as the subregions labeled A (Bengbu and Huainan City) and B (Nanjing Metropolitan Area), had lower O_3 levels than their surrounding areas. On the contrary, the subregions labeled C (Anqing City) and D (Quzhou and Jinhua City) were more polluted than their surrounding areas. As shown in Figure S13, the tropospheric column NO_2 concentrations were higher in subregions A and B than in C and D.

The Long-Term Trend of O_3 in China

Figure 6 shows the long-term trend of O_3 concentrations in the O_3 season (defined as March–November) in China. Before 2014, mean O_3 concentrations during the O_3 season fluctuated from year to year but generally stayed at the same level nationally, at $\sim$90 $\mu g/m^3$. O_3 levels in the NCP, YRD, and PRD regions were higher than the national average but were also stable around their respective long-term averages. A sharp decrease was observed in the YRD and PRD from 2014 to 2016. After 2016, O_3 levels nationwide started to rise at various paces. For example, seasonal mean O_3 concentrations were almost identical for the YRD and NCP before 2014, but the former experienced a sharper increase from 2015 to 2019 owing to the significant drop from 2014 to 2015. After 2018, the mean MDA8 O_3 concentrations in the O_3 season exceeded 100 $\mu g/m^3$ in all these regions.

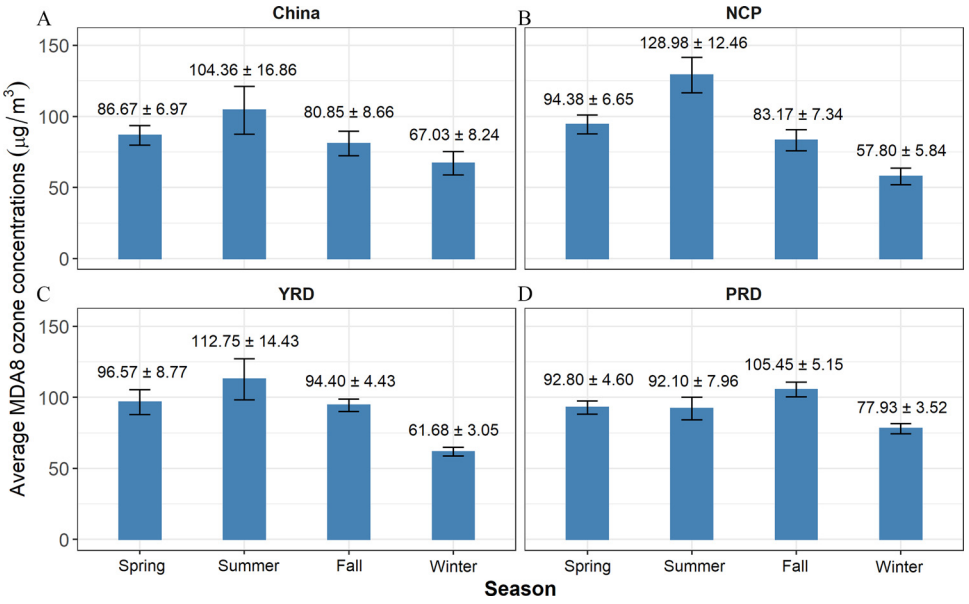

Figure 4. Region-specific seasonal mean MDA8 O_3 concentrations during 2005–2019 for (A) China as a whole, (B) the North China Plain (NCP), (C) the Yangtze River Delta region (YRD), and (D) the Pearl River Delta (PRD). The O_3 concentrations were predicted by the original model with OMI L24 retrievals. The bars and the corresponding numbers represent the season-specific regional mean MDA8 O_3 concentrations (±standard deviation) over 2005–2019. Note: Fall, September–October–November; MDA8, daily maximum 8-h average; O_3, ozone; OMI, Ozone Monitoring Instrument; spring, March–April–May; summer, June–July–August; winter, December–January–February.

Summertime (June–July–August) mean MDA8 O_3 concentrations showed an overall increasing trend during 2005–2019 in the whole of China (0.27 $\mu g/m^3$ per year, $p = 0.004$), the NCP (1.10 $\mu g/m^3$ per year, $p = 0.002$), and the YRD (0.85 $\mu g/m^3$ per year, $p = 0.010$) (Figure S14). However, similar to the O_3 season averages, no significant trend was observed for summertime mean MDA8 O_3 concentrations over 2005–2013 (0.04 $\mu g/m^3$ per year, $p = 0.789$; −0.00 $\mu g/m^3$ per year, $p = 0.990$; 0.15 $\mu g/m^3$ per year, $p = 0.700$; and 0.17 $\mu g/m^3$ per year, $p = 0.711$ for the whole of China, the NCP, the YRD, and the PRD, respectively) (Figure S15). The NCP was the only region that had an overall increasing springtime O_3 pollution over 2005–2019 (0.31 $\mu g/m^3$ per year, $p = 0.047$) (Figure S16), whereas no significant trend was found for 2005–2013 across China (−0.04 $\mu g/m^3$ per year, $p = 0.772$; −0.21 $\mu g/m^3$ per year, $p = 0.400$; −0.51 $\mu g/m^3$ per year, $p = 0.354$; and 0.02 $\mu g/m^3$ per year, $p = 0.967$ for the whole of China, the NCP, the YRD, and the PRD, respectively) (Figure S17). As shown in Table S2,

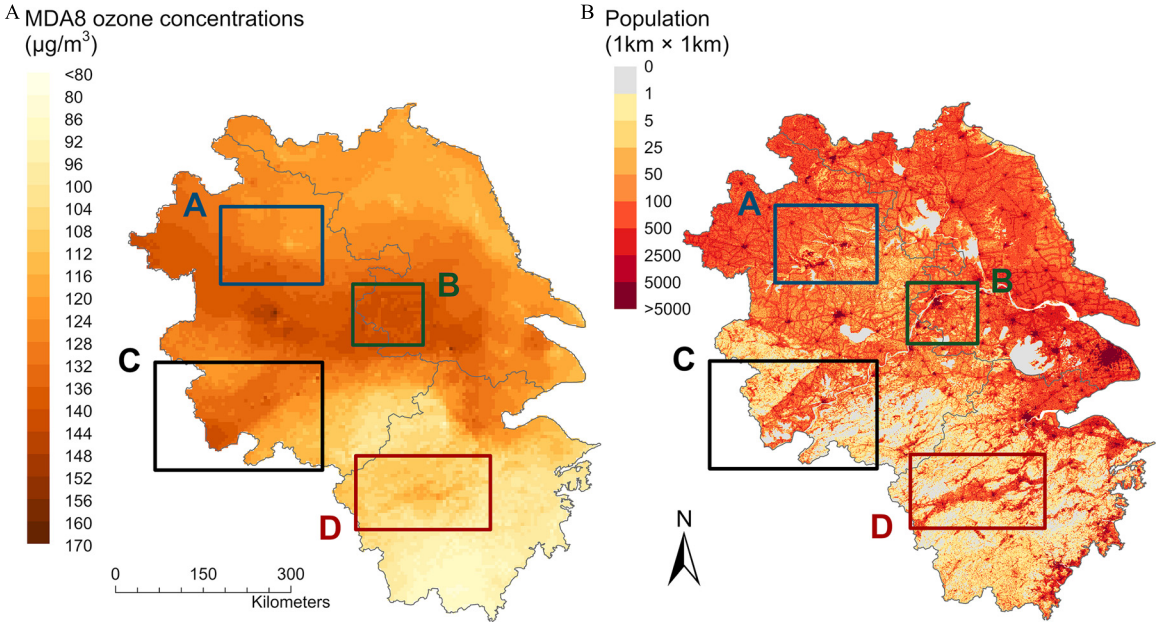

Figure 5. Summer O_3 peak and population in the Yangtze River Delta (August 2019). (A) The model-predicted monthly mean MDA8 O_3 concentrations in August 2019; and (B) the 1-km population data for 2019 from LandScan. The boxes represent some YRD cities and their surrounding areas: A, Bengbu and Huainan City; B, Nanjing Metropolitan Area; C, Anqing City; and D, Quzhou and Jinhua City. Note: MDA8, daily maximum 8-h average; O_3, ozone; YRD, the Yangtze River Delta.

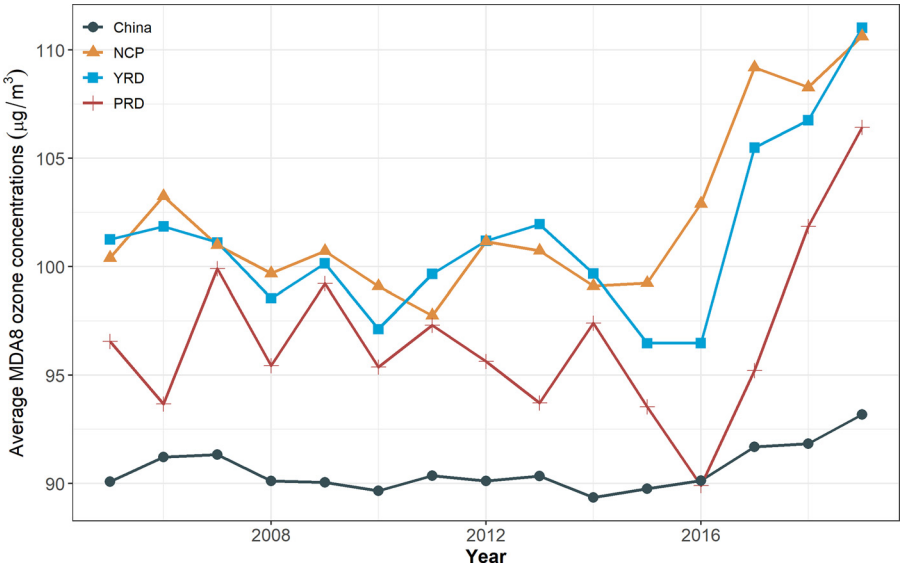

Figure 6. Annual trend of mean O_3 season average MDA8 O_3 concentrations from 2005 to 2019. O_3 season is defined as March–November. The lines with different colors and marks represent the model-predicted mean MDA8 O_3 concentrations in different regions. Gray line with round marks denotes China; the red line with cross marks, the PRD; the orange line with triangular marks, the NCP; and the blue line with square marks, the YRD. Note: MDA8, daily maximum 8-h average; NCP, the North China Plain; O_3, ozone; PRD, the Pearl River Delta; YRD, the Yangtze River Delta.

the TOAR monitoring data also did not exhibit a significant increasing trend in O_3 pollution during 2005–2013 except for the summertime pollution at the SDZ station (5.79 $\mu g/m^3$ per year, $p = 0.033$).

The predicted temporal trend was similar to the CNEMC observations over the grid cells with monitoring sites (Figure S18). Although our model may slightly underestimate the overall O_3 season MDA8 O_3 concentrations in China, the predicted summer peak O_3 concentration was almost identical with the CNEMC observations in China as a whole, as well as with the NCP, YRD, and PRD (Figure S19). Unlike our model predictions, the 2018–2019 increase in the O_3-season mean MDA8 O_3 concentrations was not seen from the CNEMC data except for the PRD. However, there was a substantial increase in some subregions, including Central-East China (Figure 7A) and the Shandong Peninsula (locations listed on Figure S20; Figure 7B), as observed by both the CNEMC data and our predictions.

Couple Trend between $PM_{2.5}$ and O_3 in China

The temporal trends of population-weighted O_3 and $PM_{2.5}$ concentrations in China and three major regions are shown in Figure 8A–D. Despite the visible inverse correlation between $PM_{2.5}$ and O_3 levels, partial correlation analyses controlling for temperature, relative humidity, and precipitation indicated that their association varied by region. A statistically significant negative correlation was observed in the YRD region ($r = -0.31$, $p < 0.001$), whereas in the PRD region, this correlation turned positive ($r = 0.34$, $p < 0.001$). No significant association was observed in China as a whole ($r = 0.03$, $p = 0.385$) and in the NCP ($r = -0.07$, $p = 0.358$) after we controlled for temperature, relative humidity, and precipitation.

Discussion

In the present study, we trained a random forest model to predict long-term ground-level MDA8 O_3 concentrations in China. To our best knowledge, our model's performance was the highest among similar studies in China. For example, the 0.1° model established by Liu et al. (2020) had a spatial CV R^2 of 0.68 and a temporal CV R^2 of 0.69 for monthly mean MDA8 O_3 concentrations. Compared with their study, our model had a finer spatial resolution (0.05°) and higher spatial and temporal CV R^2 values (0.86 and 0.76, respectively). Despite a coarser spatiotemporal resolution, our model generally had a comparable performance with those established in regions with sufficient historical O_3 monitoring data. For instance, the R^2 for daily MDA8 O_3 by Di et al. (2017) ranged from 0.7 to 0.8 across the United States over 2000–2012, and the land-use regression model of Adam-Poupart et al. (2014) had an R^2 of 0.65 for daytime 8-h average O_3 concentrations in Quebec, Canada. One reason for the improved performance was the inclusion of the OMPROFOZ O_3 profile instead of the total O_3 column. The latter is a noisy proxy for surface-level O_3 because approximately 90% of the atmospheric O_3 exists in the stratosphere (Fishman and Larsen 1987). Although the gap-filled boundary-layer O_3 column was not among the top predictors for the non-spring model, it was an important predictor in springtime when ground-level O_3 pollution is greatly influenced by SI and foreign transport (Figure S12). Another reason for the higher performance of our model is that the two primary sources of ground-level O_3 (i.e., photochemical reactions and SI) were both accounted for in our study, whereas previous studies typically focused on the impact of photochemical reactions on O_3 patterns.

With the improved spatial resolution, we were able to observe the complex relationship between human activities and O_3 concentrations, as presented in Figure 5. These regions have been reported to have a high NO_x/VOC ratio so that the abundance of VOCs controls the ambient O_3 concentrations (Liu et al. 2010b). Under the VOC-limited regime, the excessive NO_x concentrations would quench O_3 molecules through NO_x titration (Jhun et al. 2015). On the other hand, O_3 concentration in regions C (Anqing City) and D (Quzhou and Jinhua City), with moderate NO_x concentrations (Figure S13), fall under the NO_x-limited regime, with a positive association between O_3 and NO_x concentrations.

Our modeling results indicated that the seasonality of O_3 concentrations in China varied across different regions and was more distinct in northern China than in the south (Figures 3 and 4). This phenomenon could be explained by three reasons. First, the absolute and relative abundance of O_3 precursors have a major impact on O_3 concentration. The observed regional and national O_3 hot spots occurred predominantly in the megacity clusters

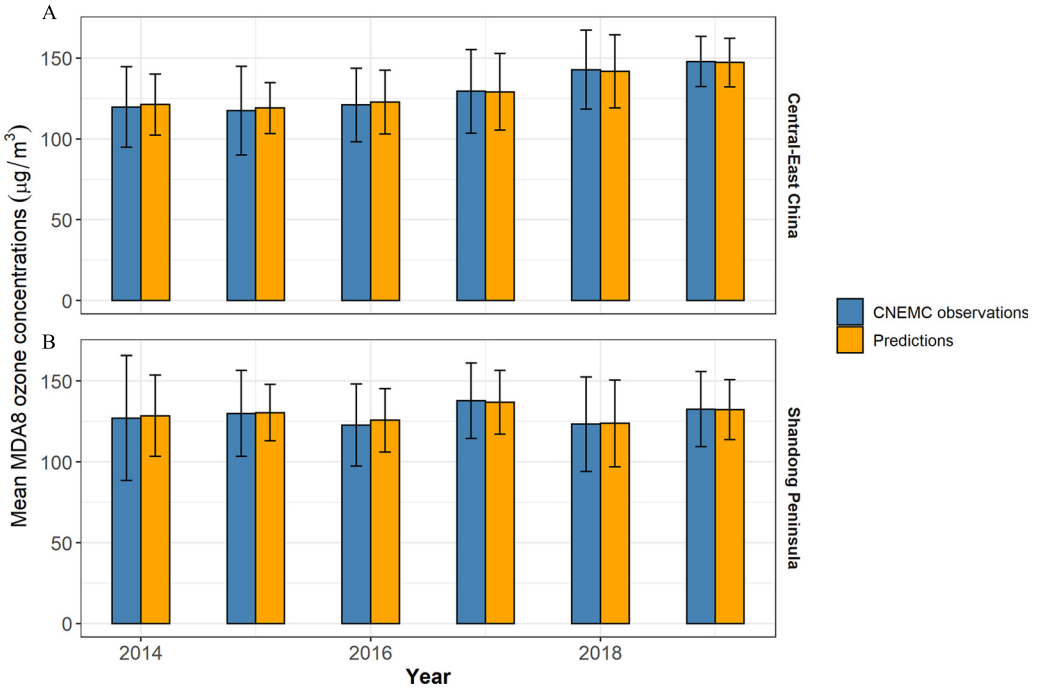

Figure 7. The comparison of the summertime (June–July–August) mean MDA8 O_3 concentrations between our model predictions and the CNEMC monitoring data over 2014–2019 for selected regions. (A) Central-East China; and (B) the Shandong Peninsula. The blue columns represent the CNEMC observations, and the orange columns represent our model predictions. The height of the columns and the error bars represent the mean MDA8 O_3 concentrations and the standard errors. Note: CNEMC, China National Environmental Monitoring Center; MDA8, daily maximum 8-h average; NCP, the North China Plain; O_3, ozone; PRD, the Pearl River Delta, YRD: the Yangtze River Delta.

(NCP, YRD, PRD, and Sichuan Basin), which can be partially attributed to high anthropogenic emissions of NO_x and VOCs (Li et al. 2019b). Second, meteorological conditions, such as temperature and solar radiation, significantly affect surface O_3 formation (Coates et al. 2016; Schnell et al. 2009), making summer the most polluted season in most regions. However, the active monsoon activities in summer, especially in the PRD, may increase cloud cover and weaken solar radiation. O_3 formation would be restrained under such a condition (Qu et al. 2021). The heavy rainfall during the monsoon season may also lead to a reduction in surface O_3 pollution. This may help explain the absence of summer O_3 peaks in the low-latitude areas, including the

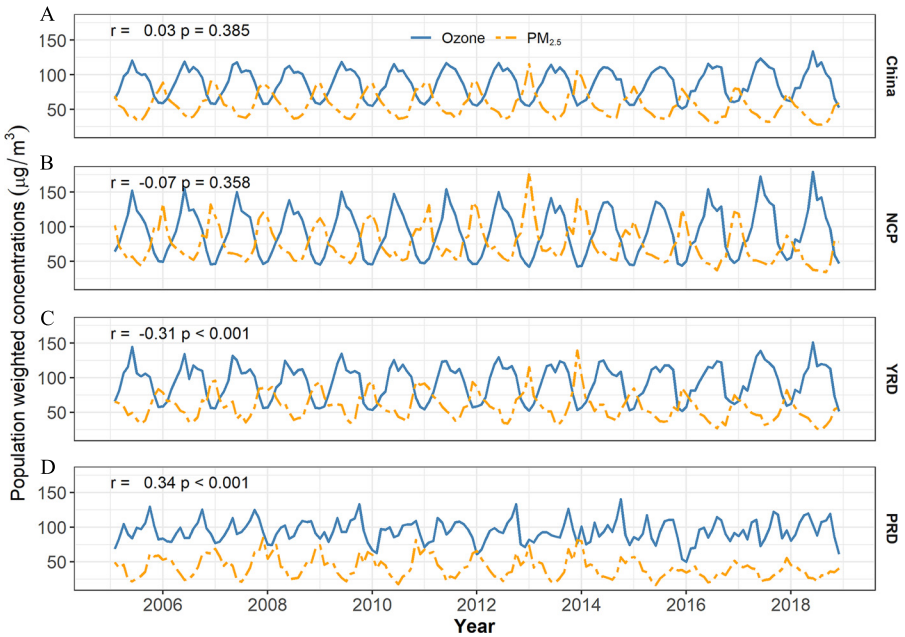

Figure 8. Time-series comparison for population-weighted ambient O_3 and $PM_{2.5}$ concentrations in China over 2005–2018. (A) China as a whole; (B) the NCP; (C) the YRD; and (D) the PRD. r denotes the partial correlation coefficient controlling for temperature, relative humidity, and total precipitation from MERRA-2. *p*-Values were for the r statistics. Blue lines represent the population-weighted monthly mean MDA8 O_3 predicted by our model, and the orange lines represent the population-weighted monthly mean $PM_{2.5}$ concentrations from Xiao et al. (2021). Note: MDA8, daily maximum 8-h average; MERRA-2, Modern-Era Retrospective Analysis for Research and Applications; NCP, the North China Plain; O_3, ozone; PRD, the Pearl River Delta; YRD, the Yangtze River Delta.

PRD. The stronger seasonal variation of solar radiation in high-latitude regions may have contributed to a shorter, but more distinct, O_3 season in the NCP. Finally, the intensity of the SI events varies by region. Deep SI events occur more frequently in the high-altitude regions, with some even reaching the ground (Lin et al. 2012, 2016). Consequently, high O_3 concentrations could be observed on the Qinghai-Tibetan plateau in spring despite lower levels of O_3 precursors and relatively low temperatures.

Although our model generally captured the seasonal variation of O_3 in China, we still found a substantial underestimation of high springtime O_3 concentrations, especially at the XGLL station (Figure S7). A potential reason for this underestimation is that foreign O_3 transport was not well accounted for in our model. According to Ni et al. (2018) foreign regions contribute 40–60% to China's springtime O_3 below the height of 2 km. This enhancement is very prominent in Southwest China owing to the massive biomass burning in South and Southeast Asia (Wang et al. 2011), which peaked in spring (Yin 2020). However, incorporating wildfire emissions from South and Southeast Asia by assuming a distance-dependent influence did not address this underestimation (Figure S8). According to Wang et al. (2011), the prevailing westerly wind and active cyclonic activity in spring facilitate O_3 transport from South Asia to China. Therefore, foreign wildfire's impact on China's O_3 pollution is not determined by distance itself but, rather, follows a certain trajectory. We are unable to address this trajectory in the current model because the grid cells did not extend outside China's boundary except for the 50-km buffer.

China has experienced rapid economic growth over the past decades. Nevertheless, the contemporary increase in anthropogenic emissions also greatly exacerbated air pollution over the nation. According to Lin et al. (2017), the 95th percentile summer (June–July–August) MDA8 O_3 increased by 1–2 ppb/y in China over 1995–2014 and the springtime (March–April–May) median O_3 increased by ~ 0.5 ppb/y concurrently. We also observed an overall increasing trend in summertime O_3 pollution during 2005–2019 in the whole of China, the NCP, and the YRD, as well as an increase in springtime O_3 pollution in the NCP (Figures S14 and S16). However, the increasing trend was not constant from year to year. As seen from our model predictions, neither the springtime nor the summer surface O_3 concentrations in China exhibited a significant increasing trend over 2005–2013 (Figures S15 and S17). These findings were mostly consistent with the TOAR monitoring data (Table S2). SDZ was the only TOAR station that observed an increasing trend in summertime O_3 pollution over 2005–2013. The increasing trend at SDZ was primarily driven by an increase from 2005–2007, whereas no significant trend was observed for 2008–2013 (1.30 $\mu g/m^3$ per year, $p = 0.735$). Xu et al. (2020) also showed that both the annual highest MDA8 O_3 and the annual fourth highest MDA8 O_3 exhibited no significant long-term increasing trend for most TOAR stations, except for SDZ. Although historical monitoring data were lacking back to the early 2000s, it can be inferred that the overall increasing trend of China's O_3 pollution during 1995–2014 was primarily driven by an increase before 2005. Tang et al. (2009) also reported that the O_3 concentrations in Beijing increased at a rate of 1.1 ppbv/y during 2001–2006. The differential trends of O_3 pollution between 1995–2004 and 2005–2013 were possibly attributable to meteorological conditions. According to Sun and Wang (2017), the surface temperature in Northern and Northeastern China increased during the 1990s but stabilized during 2005–2014.

A sharp decrease in O_3 concentration was observed in China during 2014–2016, especially in the PRD region. This was not an isolated event in China given that the U.S. Environmental Protection Agency also reported the second-lowest O_3 concentrations on record during the 2014–2016 average period (U.S. EPA 2017). The significant reduction in O_3 concentration in the northern hemisphere was attributable to El Niño during this period. Olsen et al. (2016) reported that the anomalous cyclonic circulation induced by El Niño events coincided with decreased tropospheric O_3. Shen and Mickley (2017) found a negative association between the El Niño–Southern Oscillation (ENSO) and summertime O_3 air quality in the south-central states of the United States. Although the effect of the ENSO on O_3 pollution in China has yet to be fully understood, indirect evidence supported the strong impact of climate factors between 2014 and 2016. Yang et al. (2019) reported that meteorological conditions contributed to a 10-$\mu g/m^3$ decrease of surface O_3 in 2016 and a 3- to 5-$\mu g/m^3$ decrease in 2014–2015 in the PRD region.

O_3 levels in China increased rapidly after 2016 (Figure 6). This may have to do with both China's emission control policies and meteorological conditions. The issuance of APPCAP in 2013 resulted in a dramatic nationwide decrease in NO_x emissions and $PM_{2.5}$ levels near the end of this 5-y plan (Zheng et al. 2018). However, O_3 formation falls under the VOC-limited regime in most Chinese urban centers. Reducing NO_x emissions became an enhancer of O_3 formation in populous areas, which were then transported to other regions (Liu and Wang 2020). In addition, lower $PM_{2.5}$ levels would modify O_3 pollution because the photolysis rates were less attenuated by aerosol light scattering and absorption (Liu and Wang 2020). Decreased $PM_{2.5}$ concentrations could also slow down the sink of hydroperoxyl (HO_2) radicals, resulting in enhanced O_3 production (Li et al. 2019b). Such complex interactions among O_3 formation, $PM_{2.5}$ levels, and meteorological conditions are reflected in the spatially varying associations between O_3 and $PM_{2.5}$ concentrations revealed by our partial correlation analysis. The mild weather and year-round intensive human activities cause a long O_3 season (March–November) in the YRD. During this period, $PM_{2.5}$ levels can vary from 25 to >60 $\mu g/m^3$, allowing it to affect O_3 production negatively. The PRD region was the cleanest affluent city cluster in China in terms of both $PM_{2.5}$ and O_3. The effect of $PM_{2.5}$ on O_3 production was less notable, and $PM_{2.5}$ and O_3 concentrations were both positively correlated to the emissions of their precursors (Liu and Wang 2020). Although $PM_{2.5}$ levels in the NCP are high in winter, its cold winter strongly suppresses O_3 formation, and no significant correlation was found between $PM_{2.5}$ and O_3 levels after controlling for meteorological conditions. The 2018–2019 increase in surface O_3 pollution in China was more likely to be driven by climatological factors, particularly the increased foehn wind frequency and the subsequent changes in temperature and relative humidity (Li et al. 2020). That explained why this round of increase was only seen in several regions by the CNEMC monitoring data (Figure 7). Again, although O_3 pollution in China is not consistently worsening from year to year as a result of the modulation of climatological factors, it generally exhibited a prominent long-term increasing trend (Lin et al. 2017; Xu et al. 2020). Controlling O_3 pollution in China remains a challenging task that requires a better understanding of this air pollutant.

Our study has a few limitations. First, the road network data was fixed over the study period. This may result in an underestimation of China's road density, especially after 2010. Although there are alternative road length data, we prefer not to mix multiple data sets with different methodologies to avoid introducing systematic errors. Second, the O_3 precursors included in our model were limited to NO_x. Satellite retrievals of VOCs are limited and often have weak signal-to-noise ratios in the boundary layer (Zhu et al. 2020). Although our current model was able to

identify regions under the VOC-limited regime of O_3 production, we will continue to explore effective indicators of ground-level VOC to improve our O_3 exposure model. Finally, the present study focused on domestic determinants of ambient O_3. The present model may underestimate O_3 pollution attributable to foreign transport. Future users of our data set should be cautious with the springtime underestimations, especially in Southwest China. The roles of long-range O_3 transport from outside China warrants further investigation.

Conclusions

We used a data-driven modeling framework to estimate long-term, high-resolution O_3 concentrations in China. Predictors that capture the influence of O_3 photochemical reactions and SI were included in our model. This model produced reliable historical monthly mean MDA8 O_3 concentrations for China at a 0.05° resolution with little bias. This 15-y long, full-coverage national data set of ambient O_3 concentrations includes the 9 y before China's regulatory air quality monitoring network existed. It could accelerate research on the long-term O_3 health effects in China by enabling the use of large general population cohorts established in the 2000s, such as the Chinese Longitudinal Healthy Longevity Survey (Kuang et al. 2020) and the China Health and Retirement Longitudinal Study (Zhao et al. 2014).

Acknowledgments

This work was supported by the National Institute of Environmental Health Sciences of the National Institutes of Health (NIH; award R01-ES027892). The content is solely the responsibility of the authors and does not necessarily represent the official views of NIH.

References

Adam-Poupart A, Brand A, Fournier M, Jerrett M, Smargiassi A. 2014. Spatiotemporal modeling of ozone levels in Quebec (Canada): a comparison of kriging, land-use regression (LUR), and combined Bayesian maximum entropy-LUR approaches. Environ Health Perspect 122(9):970–976, PMID: 24879650, https://doi.org/10.1289/ehp.1306566.

Altmann A, Toloşi L, Sander O, Lengauer T. 2010. Permutation importance: a corrected feature importance measure. Bioinformatics 26(10):1340–1347, PMID: 20385727, https://doi.org/10.1093/bioinformatics/btq134.

Anenberg S, Henze C, Tinney DK, Kinney V, Raich PL, Fann W, et al. 2018. Estimates of the global burden of ambient $PM_{2.5}$, ozone, and NO_2 on asthma incidence and emergency room visits. Environ Health Perspect 126(10):107004, PMID: 30392403, https://doi.org/10.1289/EHP3766.

Appenzeller C, Holton JR, Rosenlof KH. 1996. Seasonal variation of mass transport across the tropopause. J Geophys Res 101(D10):15071–15078, https://doi.org/10.1029/96JD00821.

Atkinson RW, Butland BK, Dimitroulopoulou C, Heal MR, Stedman JR, Carslaw N, et al. 2016. Long-term exposure to ambient ozone and mortality: a quantitative systematic review and meta-analysis of evidence from cohort studies. BMJ Open 6(2): e009493, PMID: 26908518, https://doi.org/10.1136/bmjopen-2015-009493.

Barry V, Klein M, Winquist A, Chang HH, Mulholland JA, Talbott EO, et al. 2019. Characterization of the concentration-response curve for ambient ozone and acute respiratory morbidity in 5 US cities. J Expo Sci Environ Epidemiol 29(2):267–277, PMID: 29915241, https://doi.org/10.1038/s41370-018-0048-7.

C3S (Copernicus Climate Change Service). 2021. Product User Guide and Specification: ICDR Land Cover 2016–2020. https://datastore.copernicus-climate.eu/documents/satellite-land-cover/D5.3.1_PUGS_ICDR_LC_v2.1.x_PRODUCTS_v1.1.pdf [accessed 4 August 2021].

CDS (Climate Data Store). 2021. Land cover classification gridded maps from 1992 to present derived from satellite observations. https://cds.climate.copernicus.eu/cdsapp#!/dataset/satellite-land-cover?tab=overview [accessed 21 July 2021].

CIESIN (Center for International Earth Science Information Network-Columbia University), ITOS (Information Technology Outreach Services-University of Georgia). 2013. Global Roads Open Access Data Set, Version 1 (gROADSv1). Palisades, NY: National Aeronautics and Space Administration Socioeconomic Data and Applications Center (SEDAC). https://doi.org/10.7927/H4VD6WCT [accessed 1 January 2021].

Clifton OE, Fiore AM, Massman WJ, Baublitz CB, Coyle M, Emberson L, et al. 2020. Dry deposition of ozone over land: processes, measurement, and modeling. Rev Geophys 58(1):e2019RG000670, PMID: 33748825, https://doi.org/10.1029/2019RG000670.

CNEMC (China National Environmental Monitoring Centre). 2012. Ambient Air Quality Standards. [In Chinese]. ICS 13.040.20. http://www.cnemc.cn/jcgf/dqhj/201711/W020181008687883046768.pdf [accessed 1 August 2021].

Coates J, Mar KA, Ojha N, Butler TM. 2016. The influence of temperature on ozone production under varying NO*x* conditions—a modelling study. Atmos Chem Phys 16(18):11601–11615, https://doi.org/10.5194/acp-16-11601-2016.

DeCaria AJ, Pickering KE, Stenchikov GL, Ott LE. 2005. Lightning-generated NO*x* and its impact on tropospheric ozone production: a three-dimensional modeling study of a Stratosphere-Troposphere Experiment: Radiation, Aerosols and Ozone (STERAO-A) thunderstorm. J Geophys Res 110(D14):D14303, https://doi.org/10.1029/2004JD005556.

Di Q, Rowland S, Koutrakis P, Schwartz J. 2017. A hybrid model for spatially and temporally resolved ozone exposures in the continental United States. J Air Waste Manag Assoc 67(1):39–52, PMID: 27332675, https://doi.org/10.1080/10962247.2016.1200159.

ESA (European Space Agency). 2017. *Land Cover CCI: Product User Guide, Version 2.* CCI-LC-PUGV2. maps.elie.ucl.ac.be/CCI/viewer/download/ESACCI-LC-Ph2-PUGv2_2.0.pdf [accessed 1 January 2021].

Finney DL, Doherty RM, Wild O, Young PJ, Butler A. 2016. Response of lightning NO*x* emissions and ozone production to climate change: insights from the atmospheric chemistry and climate model intercomparison project. Geophys Res Lett 43(10):5492–5500, https://doi.org/10.1002/2016GL068825.

Fischer EV, Jacob DJ, Yantosca RM, Sulprizio MP, Millet DB, Mao J, et al. 2014. Atmospheric peroxyacetyl nitrate (PAN): a global budget and source attribution. Atmos Chem Phys 14(5):2679–2698, PMID: 33758588, https://doi.org/10.5194/acp-14-2679-2014.

Fishman J, Larsen JC. 1987. Distribution of total ozone and stratospheric ozone in the tropics: implications for the distribution of tropospheric ozone. J Geophys Res 92(D6):6627–6634, https://doi.org/10.1029/JD092iD06p06627.

Gelaro R, McCarty W, Suárez MJ, Todling R, Molod A, Takacs L, et al. 2017. The Modern-Era Retrospective Analysis for Research and Applications, Version 2 (MERRA-2). J Clim 30(14):5419–5454, PMID: 32020988, https://doi.org/10.1175/JCLI-D-16-0758.1.

Hayashida S, Liu X, Ono A, Yang K, Chance K. 2015. Observation of ozone enhancement in the lower troposphere over East Asia from a space-borne ultraviolet spectrometer. Atmos Chem Phys 15(17):9865–9881, https://doi.org/10.5194/acp-15-9865-2015.

Huang G, Liu X, Chance K, Yang K, Bhartia PK, Cai Z, et al. 2017. Validation of 10-year SAO OMI Ozone Profile (PROFOZ) product using ozonesonde observations. Atmos Meas Tech 10(7):2455–2475, https://doi.org/10.5194/amt-10-2455-2017.

Huang J, Pan X, Guo X, Li G. 2018. Health impact of China's Air Pollution Prevention and Control Action Plan: an analysis of national air quality monitoring and mortality data. Lancet Planet Health 2(7):e313–e323, PMID: 30074894, https://doi.org/10.1016/S2542-5196(18)30141-4.

Itahashi S, Mathur R, Hogrefe C, Zhang Y. 2020. Modeling stratospheric intrusion and trans-Pacific transport on tropospheric ozone using hemispheric CMAQ during April 2010—part 1: model evaluation and air mass characterization for stratosphere–troposphere transport. Atmos Chem Phys 20(6):3373–3396, PMID: 32328089, https://doi.org/10.5194/acp-20-3373-2020.

Jhun I, Coull BA, Zanobetti A, Koutrakis P. 2015. The impact of nitrogen oxides concentration decreases on ozone trends in the USA. Air Qual Atmos Health 8(3):283–292, PMID: 27547271, https://doi.org/10.1007/s11869-014-0279-2.

Kang D, Mathur R, Pouliot GA, Gilliam RC, Wong DC. 2020. Significant ground-level ozone attributed to lightning-induced nitrogen oxides during summertime over the Mountain West States. NPJ Clim Atmos Sci 3:6, PMID: 32181370, https://doi.org/10.1038/s41612-020-0108-2.

Kigathi RN, Weisser WW, Reichelt M, Gershenzon J, Unsicker SB. 2019. Plant volatile emission depends on the species composition of the neighboring plant community. BMC Plant Biol 19(1):58, PMID: 30727963, https://doi.org/10.1186/s12870-018-1541-9.

Kim PS, Jacob DJ, Liu X, Warner JX, Yang K, Chance K, et al. 2013. Global ozone–CO correlations from OMI and AIRS: constraints on tropospheric ozone sources. Atmos Chem Phys 13(18):9321–9335, https://doi.org/10.5194/acp-13-9321-2013.

Knowland KE, Ott LE, Duncan BN, Wargan K. 2017. Stratospheric intrusion-influenced ozone air quality exceedances investigated in the NASA MERRA-2 reanalysis. Geophys Res Lett 44(20):10691–10701, PMID: 32692318, https://doi.org/10.1002/2017gl074532.

Krotkov NA, Lamsal LN, Celarier EA, Swartz WH, Marchenko SV, Bucsela EJ, et al. 2017. The version 3 OMI NO_2 standard product. Atmos Meas Tech 10(9):3133–3149, https://doi.org/10.5194/amt-10-3133-2017.

Kuang W, Gao M, Tian L, Wan Y, Qiu P. 2020. Trends in the prevalence of cognitive impairment in Chinese older adults: based on the Chinese Longitudinal Healthy

Longevity Survey cohorts from 1998 to 2014. Int Health 12(5):378–387, PMID: 31967316, https://doi.org/10.1093/inthealth/ihz114.
Lelieveld J, Dentener FJ. 2000. What controls tropospheric ozone? J Geophys Res 105(D3):3531–3551, https://doi.org/10.1029/1999JD901011.
Levelt PF, van den Oord GHJ, Dobber MR, Malkki A, Huib V, de Vries J, et al. 2006. The Ozone Monitoring Instrument. IEEE Trans Geosci Remote Sens 44(5):1093–1101, https://doi.org/10.1109/TGRS.2006.872333.
Li F, Zhang X, Roy DP, Kondragunta S. 2019a. Estimation of biomass-burning emissions by fusing the fire radiative power retrievals from polar-orbiting and geostationary satellites across the conterminous United States. Atmos Environ 211:274–287, https://doi.org/10.1016/j.atmosenv.2019.05.017.
Li K, Jacob DJ, Liao H, Shen L, Zhang Q, Bates KH. 2019b. Anthropogenic drivers of 2013–2017 trends in summer surface ozone in China. Proc Natl Acad Sci U S A 116(2):422–427, PMID: 30598435, https://doi.org/10.1073/pnas.1812168116.
Li K, Jacob DJ, Shen L, Lu X, De Smedt I, Liao H. 2020. Increases in surface ozone pollution in China from 2013 to 2019: anthropogenic and meteorological influences. Atmos Chem Phys 20(19):11423–11433, https://doi.org/10.5194/acp-20-11423-2020.
Liang F, Xiao Q, Huang K, Yang X, Liu F, Li J, et al. 2020. The 17-y spatiotemporal trend of $PM_{2.5}$ and its mortality burden in China. Proc Natl Acad Sci USA 117(41):25601–25608, PMID: 32958653, https://doi.org/10.1073/pnas.1919641117.
Lin M, Fiore AM, Cooper OR, Horowitz LW, Langford AO, Levy IIH, et al. 2012. Springtime high surface ozone events over the Western United States: quantifying the role of stratospheric intrusions. J Geophys Res 117(D21):D00V22, https://doi.org/10.1029/2012JD018151.
Lin M, Horowitz LW, Payton R, Fiore AM, Tonnesen G. 2017. US surface ozone trends and extremes from 1980 to 2014: quantifying the roles of rising Asian emissions, domestic controls, wildfires, and climate. Atmos Chem Phys 17(4):2943–2970, https://doi.org/10.5194/acp-17-2943-2017.
Lin M, Su L, Shaheen R, Fung JCH, Thiemens MH. 2016. Detection of deep stratospheric intrusions by cosmogenic ^{35}S. Proc Natl Acad Sci U S A 113(40):11131–11136, PMID: 27655890, https://doi.org/10.1073/pnas.1609919113.
Liu R, Ma Z, Liu Y, Shao Y, Zhao W, Bi J. 2020. Spatiotemporal distributions of surface ozone levels in China from 2005 to 2017: a machine learning approach. Environ Int 142:105823, PMID: 32521347, https://doi.org/10.1016/j.envint.2020.105823.
Liu X, Bhartia PK, Chance K, Spurr RJD, Kurosu TP. 2010a. Ozone profile retrievals from the Ozone Monitoring Instrument. Atmos Chem Phys 10(5):2521–2537, https://doi.org/10.5194/acp-10-2521-2010.
Liu XH, Zhang Y, Xing J, Zhang Q, Wang K, Streets DG, et al. 2010b. Understanding of regional air pollution over China using CMAQ, part II. Process analysis and sensitivity of ozone and particulate matter to precursor emissions. Atmos Environ 44(30):3719–3727, https://doi.org/10.1016/j.atmosenv.2010.03.036.
Liu Y, Wang T. 2020. Worsening urban ozone pollution in China from 2013 to 2017—part 2: the effects of emission changes and implications for multi-pollutant control. Atmos Chem Phys 20(11):6323–6337, https://doi.org/10.5194/acp-20-6323-2020.
Lu X, Zhang L, Chen Y, Zhou M, Zheng B, Li K, et al. 2019a. Exploring 2016–2017 surface ozone pollution over China: source contributions and meteorological influences. Atmos Chem Phys 19(12):8339–8361, https://doi.org/10.5194/acp-19-8339-2019.
Lu X, Zhang L, Shen L. 2019b. Meteorology and climate influences on tropospheric ozone: a review of natural sources, chemistry, and transport patterns. Curr Pollut Rep 5(4):238–260, https://doi.org/10.1007/s40726-019-00118-3.
Lu X, Zhang L, Wang X, Gao M, Li K, Zhang Y, et al. 2020. Rapid increases in warm-season surface ozone and resulting health impact in China since 2013. Environ Sci Technol Lett 7(4):240–247, https://doi.org/10.1021/acs.estlett.0c00171.
Lu X, Zhang L, Yue X, Zhang J, Jaffe DA, Stohl A, et al. 2016. Wildfire influences on the variability and trend of summer surface ozone in the mountainous western United States. Atmos Chem Phys 16(22):14687–14702, https://doi.org/10.5194/acp-16-14687-2016.
Lyu C, Capps SL, Hakami A, Zhao S, Resler J, Carmichael GR, et al. 2019. Elucidating emissions control strategies for ozone to protect human health and public welfare within the continental United States. Environ Res Lett 14(12):124093, https://doi.org/10.1088/1748-9326/ab5e05.
Monks PS. 2005. Gas-phase radical chemistry in the troposphere. Chem Soc Rev 34(5):376–395, PMID: 15852151, https://doi.org/10.1039/b307982c.
Murray LT, Jacob DJ, Logan JA, Hudman RC, Koshak WJ. 2012. Optimized regional and interannual variability of lightning in a global chemical transport model constrained by LIS/OTD satellite data. J Geophys Res 117(D20):D20307, https://doi.org/10.1029/2012JD017934.
NASA Earthdata (National Aeronautics and Space Administration Earthdata). 2019. MODIS Collection 6 Hotspot/Active Fire Detections MCD14ML distributed from NASA FIRMS. https://firms.modaps.eosdis.nasa.gov/download/ [accessed 15 July 2021].
NASA, METI (Japan's Ministry of Economy, Trade, and Industry). 2019. ASTGTM v003: ASTER Global Digital Elevation Model 1 arc second, https://doi.org/10.5067/ASTER/ASTGTM.003 [accessed 1 January 2021].
NBS (National Bureau of Statistics). 2008. Appendix 7: Provisions on the Statistical Division of Urban and Rural Areas (for Trial Implementation). [In Chinese]. http://www.stats.gov.cn/tjsj/pcsj/rkpc/5rp/html/append7.htm [accessed 26 July 2021].
Ni R, Lin J, Yan Y, Lin W. 2018. Foreign and domestic contributions to springtime ozone over China. Atmos Chem Phys 18(15):11447–11469, https://doi.org/10.5194/acp-18-11447-2018.
Nuvolone D, Petri D, Voller F. 2018. The effects of ozone on human health. Environ Sci Pollut Res Int 25(9):8074–8088, PMID: 28547375, https://doi.org/10.1007/s11356-017-9239-3.
Olsen MA, Wargan K, Pawson S. 2016. Tropospheric column ozone response to ENSO in GEOS-5 assimilation of OMI and MSL ozone data. Atmos Chem Phys 16(11):7091–7103, https://doi.org/10.5194/acp-16-7091-2016.
Pu X, Wang TJ, Huang X, Melas D, Zanis P, Papanastasiou DK, et al. 2017. Enhanced surface ozone during the heat wave of 2013 in Yangtze River Delta region. Sci Total Environ 603–604:807–816, PMID: 28442137, https://doi.org/10.1016/j.scitotenv.2017.03.056.
Qu K, Wang X, Yan Y, Shen J, Xiao T, Dong H, et al. 2021. A comparative study to reveal the influence of typhoons on the transport, production and accumulation of O_3 in the Pearl River Delta, China. Atmos Chem Phys 21(15):11593–11612, https://doi.org/10.5194/acp-21-11593-2021.
Schnell RC, Oltmans SJ, Neely RR, Endres MS, Molenar JV, White AB. 2009. Rapid photochemical production of ozone at high concentrations in a rural site during winter. Nature Geosci 2(2):120–122, https://doi.org/10.1038/ngeo415.
Seltzer KM, Shindell DT, Malley CS. 2018. Measurement-based assessment of health burdens from long-term ozone exposure in the United States, Europe, and China. Environ Res Lett 13(10):104018, https://doi.org/10.1088/1748-9326/aae29d.
Shen L, Jacob DJ, Liu X, Huang G, Li K, Liao H, et al. 2019. An evaluation of the ability of the Ozone Monitoring Instrument (OMI) to observe boundary layer ozone pollution across China: application to 2005–2017 ozone trends. Atmos Chem Phys 19(9):6551–6560, https://doi.org/10.5194/acp-19-6551-2019.
Shen L, Mickley LJ. 2017. Effects of El Niño on summertime ozone air quality in the eastern United States. Geophys Res Lett 44(24):12543–12550, PMID: 29622852, https://doi.org/10.1002/2017gl076150.
Sun B, Wang H. 2017. A trend towards a stable warm and windless state of the surface weather conditions in northern and northeastern China during 1961–2014. Adv Atmos Sci 34(6):713–726, https://doi.org/10.1007/s00376-017-6252-x.
Tang G, Li X, Wang Y, Xin J, Ren X. 2009. Surface ozone trend details and interpretations in Beijing, 2001–2006. Atmos Chem Phys 9(22):8813–8823, https://doi.org/10.5194/acp-9-8813-2009.
Turner MC, Jerrett M, Pope CA III, Krewski D, Gapstur SM, Diver WR, et al. 2016. Long-term ozone exposure and mortality in a large prospective study. Am J Respir Crit Care Med 193(10):1134–1142, PMID: 26680605, https://doi.org/10.1164/rccm.201508-1633OC.
U.S. EPA (U.S. Environmental Protection Agency). 2017. Ambient concentrations of ozone. https://cfpub.epa.gov/roe/indicator.cfm?i=8 [accessed 10 January 2021].
Wang T, Xue L, Brimblecombe P, Lam YF, Li L, Zhang L. 2017. Ozone pollution in China: a review of concentrations, meteorological influences, chemical precursors, and effects. Sci Total Environ 575:1582–1596, PMID: 27789078, https://doi.org/10.1016/j.scitotenv.2016.10.081.
Wang Y, Gao W, Wang S, Song T, Gong Z, Ji D, et al. 2020a. Contrasting trends of $PM_{2.5}$ and surface-ozone concentrations in China from 2013 to 2017. Natl Sci Rev 7(8):1331–1339, PMID: 34692161, https://doi.org/10.1093/nsr/nwaa032.
Wang Y, Wang H, Wang W. 2020b. A stratospheric intrusion-influenced ozone pollution episode associated with an intense horizontal-trough event. Atmosphere 11(2):164, https://doi.org/10.3390/atmos11020164.
Wang Y, Zhang Y, Hao J, Luo M. 2011. Seasonal and spatial variability of surface ozone over China: contributions from background and domestic pollution. Atmos Chem Phys 11(7):3511–3525, https://doi.org/10.5194/acp-11-3511-2011.
Wargan K, Labow G, Frith S, Pawson S, Livesey N, Partyka G. 2017. Evaluation of the ozone fields in NASA's MERRA-2 reanalysis. J Clim 30(8):2961–2988, PMID: 29527096, https://doi.org/10.1175/JCLI-D-16-0699.1.
Wooster MJ, Zhukov B, Oertel D. 2003. Fire radiative energy for quantitative study of biomass burning: derivation from the BIRD experimental satellite and comparison to MODIS fire products. Remote Sens Environ 86(1):83–107, https://doi.org/10.1016/S0034-4257(03)00070-1.
Xiao Q, Geng G, Liang F, Wang X, Lv Z, Lei Y, et al. 2020. Changes in spatial patterns of $PM_{2.5}$ pollution in China 2000–2018: impact of clean air policies. Environ Int 141:105776, PMID: 32402983, https://doi.org/10.1016/j.envint.2020.105776.
Xiao Q, Liang F, Ning M, Zhang Q, Bi J, He K, et al. 2021. The long-term trend of $PM_{2.5}$-related mortality in China: the effects of source data selection. Chemosphere 263:127894, PMID: 32814138, https://doi.org/10.1016/j.chemosphere.2020.127894.
Xie F, Li J, Tian W, Zhang J, Shu J. 2014. The impacts of two types of El Niño on global ozone variations in the last three decades. Adv Atmos Sci 31(5):1113–1126, https://doi.org/10.1007/s00376-013-3166-0.
Xu X, Lin W, Xu W, Jin J, Wang Y, Zhang G, et al. 2020. Long-term changes of regional ozone in China: implications for human health and ecosystem impacts. Elementa (Wash D C) 8:13, https://doi.org/10.1525/elementa.409.

Yang L, Luo H, Yuan Z, Zheng J, Huang Z, Li C, et al. 2019. Quantitative impacts of meteorology and precursor emission changes on the long-term trend of ambient ozone over the Pearl River Delta, China, and implications for ozone control strategy. Atmos Chem Phys 19(20):12901–12916, https://doi.org/10.5194/acp-19-12901-2019.

Yin P, Chen R, Wang L, Meng X, Liu C, Niu Y, et al. 2017. Ambient ozone pollution and daily mortality: a nationwide study in 272 Chinese cities. Environ Health Perspect 125(11):117006, PMID: 29212061, https://doi.org/10.1289/EHP1849.

Yin S. 2020. Biomass burning spatiotemporal variations over South and Southeast Asia. Environ Int 145:106153, PMID: 33002702, https://doi.org/10.1016/j.envint.2020.106153.

Zhao Y, Hu Y, Smith JP, Strauss J, Yang G. 2014. Cohort profile: the China Health and Retirement Longitudinal Study (CHARLS). Int J Epidemiol 43(1):61–68, PMID: 23243115, https://doi.org/10.1093/ije/dys203.

Zheng B, Tong D, Li M, Liu F, Hong C, Geng G, et al. 2018. Trends in China's anthropogenic emissions since 2010 as the consequence of clean air actions. Atmos Chem Phys 18(19):14095–14111, https://doi.org/10.5194/acp-18-14095-2018.

Zhu L, González Abad G, Nowlan CR, Chan Miller C, Chance K, Apel EC, et al. 2020. Validation of satellite formaldehyde (HCHO) retrievals using observations from 12 aircraft campaigns. Atmos Chem Phys 20(20):12329–12345, https://doi.org/10.5194/acp-20-12329-2020.